

Study of Excited Ξ Baryons with the $\overline{\text{PANDA}}$ Detector

Jennifer Pütz ^{*1}, Albrecht Gillitzer¹, James Ritman^{1,2}, Tobias Stockmanns¹ and the $\overline{\text{PANDA}}$ Collaboration

¹Forschungszentrum Jülich, Jülich, Germany

²Institut für Experimentalphysik, Ruhr-Universität Bochum, Universitätsstr. 150, 44780 Bochum, Germany

Abstract

The study of baryon excitation spectra provides insight into the inner structure of baryons. So far, most of the world-wide efforts have been directed towards N^* and Δ spectroscopy. Nevertheless, the study of the double and triple strange baryon spectrum will give independent information to the information deduced from the N^* and Δ spectra.

The future antiproton experiment $\overline{\text{PANDA}}$ will provide direct access to final states containing a $\Xi\Xi$ pair for which, in $\bar{p}p$ reactions, production cross sections up to the order of μb are expected. Assuming a luminosity of $L = 10^{31} \text{ cm}^{-2}\text{s}^{-1}$ in the first phase of the experiment, the expected cross sections correspond to a production rate of $\sim 10^6/\text{d}$. Combined with the nearly 4π detector acceptance, $\overline{\text{PANDA}}$ will be a hyperon factory.

In this study, reactions of the type $\bar{p}p \rightarrow \Xi^{*+} \Xi^{-}$ as well as $\bar{p}p \rightarrow \Xi^{*+} \Xi^{-}$ with various decay modes are investigated. Two different methods for the exclusive reconstruction of the signal events are presented, i.e. a step-by-step reconstruction and a full decay tree fit, resulting in reconstruction efficiencies between 3 % and 5 %. This allows to collect high statistics data within a few weeks of data taking.

^{*}j.puetz@fz-juelich.de

1 Introduction

The strong coupling constant α_s increases with decreasing momentum transfer, until at a scale of the proton radius the value of α_s is so large that perturbative methods no longer are applicable. Theoretical models have to be used, which need experimental data to constrain the used parameters [1, 2].

At low energy, the exchange of hadrons appears to describe the appropriate degrees of freedom for the excitation spectrum and the scattering cross section of baryonic resonances. For a deeper insight into the mechanism of non-perturbative QCD the understanding of the excitation pattern of baryons is essential. Hadrons are composite particles which have internal degrees of freedom and thus an excitation spectrum. This leads to two possibilities to study hadrons in experiments. One possibility is to study reaction dynamics, i.e. the investigation of hadron-hadron interactions and hadron production, while the other is hadron spectroscopy, where the structure of hadrons is investigated.

Most systematic experimental studies so far have focused on the nucleon excitation spectrum. In contrast, the knowledge is poor for excited double or triple strange baryon states, also called hyperons.

This work focuses on the spectroscopy of excited double strange hyperons. For most hyperons the spectra as well as the properties are still not well understood. $\bar{p}p$ induced reactions resulting in a baryon-antibaryon pair provide a good opportunity to access these properties and spectra, since a high fraction of the inelastic $\bar{p}p$ cross section is associated to final states with a baryon-antibaryon pair together with additional mesons. In the $\bar{p}p$ entrance channel, the production of extra strange mesons is not needed to balance the strangeness in the production of strange or multi-strange baryons. In addition, it is possible to directly populate intermediate states, where one hyperon or both hyperons are in an excited state. The excited states will predominantly give rise to final states consisting of a baryon-antibaryon pair and one or more mesons, where the produced particles may further decay weakly or electromagnetically. If the resonant states in the (anti-)baryon-meson combined system, are

sufficiently narrow, it will be possible to measure their mass and width directly. A partial wave analysis will then give the opportunity to access those observables, e.g. spin and parity quantum numbers, which are otherwise difficult to determine directly.

Comprehensive measurements will need next generation experiments. The future Antiproton Annihilation in Darmstadt (\bar{P} ANDA) experiment located at the FAIR facility will be such an experiment [3]. It will be a multi-purpose detector to study antiproton-proton induced reaction at beam energies between 1.5 GeV/c and 15 GeV/c. Therefore, \bar{P} ANDA is well-suited for a comprehensive baryon spectroscopy program in the multi-strange and charm sector. The expected cross section for final states containing a $\bar{\Xi}^+ \Xi^-$ pair is on the order of μb [4], thus giving the possibility to collect high statistics data.

This work presents a feasibility study for the reconstruction of the reaction $\bar{p}p \rightarrow \bar{\Xi}^+ \Xi^{*-}$ and its charge conjugate channel with the \bar{P} ANDA detector, where Ξ^* denotes the following intermediate resonances: $\Xi(1530)^-$, $\Xi(1690)^-$ and $\Xi(1820)^-$. Various decay modes of the resonance states are investigated.

2 \bar{P} ANDA

The \bar{P} ANDA experiment [3] will be part of the Facility for Antiproton and Ion Research (FAIR) [5]. FAIR is an international accelerator facility for the research with antiprotons and ions, which is currently under construction in Darmstadt, Germany. The facility will consist of a system of storage rings. One of these storage rings is the High Energy Storage Ring (HESR) which is optimized for high energy antiprotons and will provide a luminosity of about $10^{31} \text{ cm}^{-2} \text{ s}^{-1}$ in the first phase of operation [6]. HESR can accelerate or decelerate the antiprotons to produce a phase-space cooled beam momentum between anywhere 1.5 GeV/c and 15 GeV/c. In a later stage a peak luminosity of $2 \cdot 10^{32} \text{ cm}^{-2} \text{ s}^{-1}$ will be reached [7].

The proposed \bar{P} ANDA detector, shown in Figure 1, is a multi-purpose detector and will be an internal experiment at the HESR. It

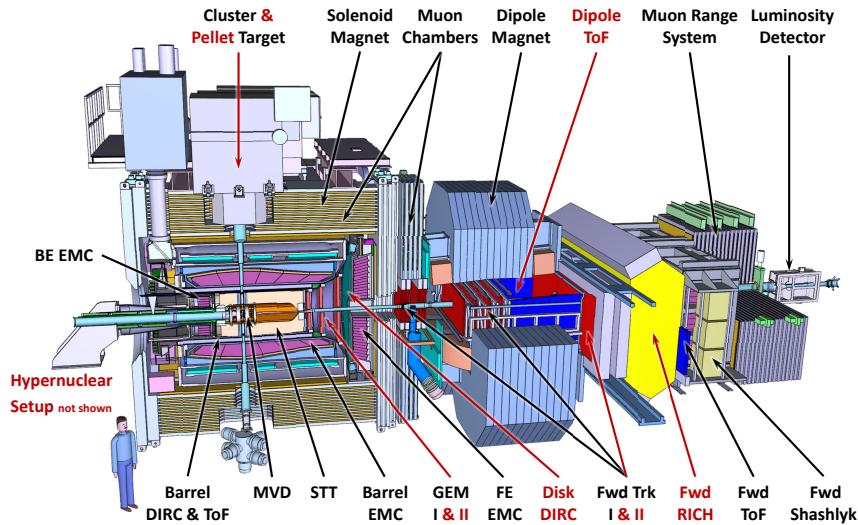


Figure 1: Schematic overview of the $\bar{\text{PANDA}}$ detector setup. The components with black labels will be available for the initial configuration of $\bar{\text{PANDA}}$ and the components with red labels will be added later. Figure taken from [8].

will be composed of two parts, the *Target Spectrometer* (TS) surrounding the interaction point (IP) and the *Forward Spectrometer* (FS). This modular design of $\bar{\text{PANDA}}$ will lead to almost 4π geometrical acceptance.

$\bar{\text{PANDA}}$ will investigate interactions between the antiproton beam and fixed target protons and/or nuclei. Reactions of the antiproton beam on fixed target protons will have a center-of-mass energy between 2.25 GeV and 5.47 GeV. The target protons will be provided either by a cluster-jet or frozen hydrogen pellets [9]. In addition, targets of other elements can also be provided for $\bar{p}A$ studies.

$\bar{\text{PANDA}}$ provides a nearly complete angular coverage, high resolutions for charged and neutral particles as well as a good particle identification. The Micro Vertex Detector (MVD) is the innermost part of the tracking system inside the *Target Spectrometer* and uses two different detector technologies: hybrid pixel detectors and double-sided micro-strip detectors [10]. The main task is to tag events with open charm and strangeness. Therefore, the MVD will provide a spatial resolution

of about $10\mu\text{m}$ perpendicular to and $100\mu\text{m}$ along the beam axis.

The main tracking detector for charged particles in the TS is the Straw Tube Tracker (STT), which consists of 4636 single straw tubes arranged in a cylindrical volume around the IP and encloses the MVD [11]. Together with the MVD and the Gaseous Electron Multiplier (GEM) planes, which are downstream of the STT. The STT is embedded inside the magnetic field of a 2 T solenoid [12] giving the possibility to measure the momentum of charged particles. A momentum resolution of $\sigma_p/p \sim 1 - 2\%$ will be provided by the charged particle target spectrometer tracking system.

The main charged particle tracking system in the FS is called the Forward Tracker (FTrk) and will consist of three pairs of tracking planes equipped with straw tubes [13]. The planes will be placed before, inside and behind a $2\text{T} \cdot \text{m}$ dipole magnet. One of the main tasks is the measurement of particles with low transverse momentum.

A good particle identification (PID) is important for the event reconstruction. Therefore,

the design of the $\bar{\text{P}}\text{ANDA}$ detector includes PID sub-detectors, i.e. Cherenkov detectors, in particular the Detection of Internal Cherenkov Light (DIRC) [14] and the Ring Imaging Cherenkov (RICH) detector, the Barrel Time of Flight (BarrelToF) [15] and the Forward Time of Flight (FTof) detector [16], and the Muon Detector System (MDS) [17].

Many channels in the $\bar{\text{P}}\text{ANDA}$ physics program have photons or electron-positron pairs in the final state. The Electromagnetic Calorimeter (EMC) will provide an efficient reconstruction of positron, electron and photons while the background will be suppressed, efficiently. In the TS the EMC will be equipped with more than 15,000 PbWO_4 crystals [18]. In the FS, a shashlyk-type calorimeter is foreseen [19]. The *Forward Spectrometer* will be completed with a Luminosity Detector (LMD) to enable cross section normalization by measuring forward elastically scattered antiprotons in the Coulomb-Nuclear interference region [20].

Software Framework

The software framework used to analyze the data is called PandaRoot and is based on ROOT [21] together with the Virtual Monte Carlo (VMC) package [22]. The simulation and reconstruction code is implemented within the FairRoot software framework [23] developed as a common computing structure for all future FAIR experiments [24]. The detector simulation is handled by VMC and allows the usage of Geant3 [25] and Geant4 [26]. Several event generators, i.e. EvtGen [27], DPM [28], UrQMD [29], Pythia [30] and Fluka [31] can be used for the production of signal and background events. Subsequently, VMC sends these events to the transport model. The detector response after the simulation and propagation of the events is simulated by digitizers.

Charged particle tracks are formed by combining the hits from the tracking detectors. For the TS tracking system, the tracking algorithms assume a constant magnetic field and thus helix trajectories for charged particles. The Kalman Filter GENFIT [32] and the track follower GEANE [33] are used to take magnetic field inhomogeneities, energy loss, small angle scattering and the error calculation for the different detector parts into account. Up to now,

the tracking algorithms use the IP as the origin of the particle track. As a consequence, the tracking algorithm has poorer performance for particles emitted far from the IP. This means that the standard tracking algorithms do not perform well for the reconstruction of hyperons, which decay with displaced vertices due to their relative long lifetime. For this case, an ideal tracking algorithm is used, which groups the hit points into a track based on the generated particle information.

The information of the PID detectors are correlated to the information coming from the reconstructed particles tracks to form charged particles. If the particle tracks are not correlated to clusters inside the EMC, neutral candidates are formed. For a fast particle identification, algorithms based on Bayesian approaches are implemented [24].

3 Event generation and Track Reconstruction & Filtering

In this section the event generation as well as the procedure for the single track reconstruction and for track filtering is presented.

3.1 Event generation

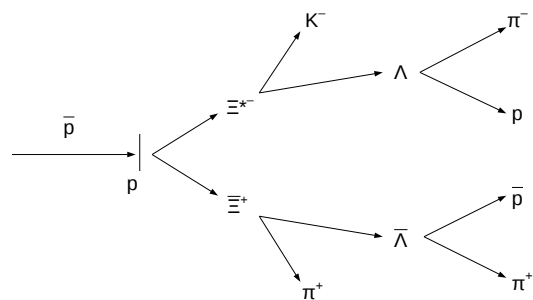


Figure 2: Decay tree for the simulation of $\bar{p} p \rightarrow \Xi^+ \Xi^{*-}$ where Ξ^* decays into ΛK^- .

In this study, the events to be analyzed, called signal events in the following, were generated with the event generator EvtGen [34] according to a defined decay chain as shown in Figure 2, for example. The antiproton momentum is chosen to be $p_{\bar{p}} = 4.6 \text{ GeV}/c$ corresponding to a center-of-mass (c.m.) energy of

$\sqrt{s} = 3.25$ GeV. The chosen beam momentum allows the population of several resonant states of the Ξ baryon, i.e. $\Xi(1530)^-$, $\Xi(1690)^-$ and $\Xi(1820)^-$ as well as $\Xi(1530)^+$, $\Xi(1690)^+$ and $\Xi(1820)^+$. The properties of the resonant states according to [35] are summarized in Table 1. Different decay channels of the Ξ resonances are investigated:

- $\Xi^{*-} \rightarrow \Lambda K^-$,
- $\Xi^{*-} \rightarrow \Xi^- \pi^0$, and
- their charge conjugate channels.

The chosen decay channels allow a good test of the reconstruction of far-off vertices (Λ), PID of rare particles (K^+ , K^-), the reconstruction of composite vertices, $\Xi^- \rightarrow \pi^- \Lambda$ followed by $\Lambda \rightarrow \pi^- p$, and also the combination of charged particle information with photon reconstruction (π^0).

Beside the resonances also a non-resonant contribution has been generated for each data sample. A full overview of the generated samples is shown in Table 2. The ratio between the resonant and non-resonant contribution to the signal events is an assumption based on measured total production cross sections of both excited and ground states of single strange hyperons in [36].

For each decay mode an isotropic angular distribution is chosen since there are neither experimental data nor theoretical predictions for the reaction $\bar{p}p \rightarrow \Xi^+ \Xi^{*-}$ and its charge conjugate reaction, respectively. This simplification ensures that both baryon and anti-baryon are underlying the same detector acceptance. In addition, the decay of each resonance is assumed to be isotropic.

Furthermore, the production cross section for $\bar{p}p \rightarrow \Xi^+ \Xi^{*-}$ as well as for $\bar{p}p \rightarrow \Xi^{*+} \Xi^-$ is

unknown. For the production of $\Xi^+ \Xi^-$ in $\bar{p}p$ collisions at $p = 3$ GeV/c beam momentum a cross section of $\sigma \simeq 2 \mu\text{b}$ has been measured [4]. In case of single strange hyperons, the comparison of the ground state and the excited state production shows similar cross section for both species [36]. Therefore, the cross section $\sigma(\bar{p}p \rightarrow \Xi^+ \Xi^{*-})$ is assumed to be of the order of $1 \mu\text{b}$.

Since EvtGen does not take into account the curved trajectory in the magnetic field of the solenoid or the interaction of particles with the detector volume, the propagation of Ξ^+ and Ξ^- is passed to Geant4.

The branching ratio for both Ξ baryons to $\Lambda\pi$ is $\text{BR}(\Xi \rightarrow \Lambda\pi) = 99.98\%$. In contrast, Λ as well as $\bar{\Lambda}$ have various decay modes with a significant branching ratio. Since this study focuses on $\Lambda \rightarrow p + \pi^-$ and $\bar{\Lambda} \rightarrow \bar{p} + \pi^+$, in Geant4, the corresponding branching ratio ($BR = 63.4\%$) is set to 100% to avoid the generation of unwanted final states. This implies that the final results have to be scaled by the correct branching ratios for further calculations.

3.2 Track Reconstruction and Filtering

A characteristic feature of ground state hyperons is their long decay time, so that they can propagate several centimeters before they decay. The lifetimes ($c\tau$) of the Λ and Ξ is 7.89 and 4.91 cm, respectively [35]. This implies, that their daughter particles are not produced closed to the interaction point. As mentioned in Section 2, the tracking algorithms in PandaRoot assume particles to come from the IP meaning that the implemented algorithms are not able to reconstruct the charged final state particles of the reactions to be studied. This implies that the usage of an ideal pattern recognition algorithm is required. As a consequence, also particles leaving only one hit in any sub-detector will be reconstructed. Therefore, a track filter is needed to reject those tracks which have a low hit multiplicity in the tracking detectors. In the following, only those charged final state particles are further considered if leave at least four hits in one of inner tracking detectors (MVD, STT or GEM). This selection criterion is motivated by the helix tra-

Table 1: Mass and width of the Ξ resonances as implemented for the event generation. The values in parentheses were used for the event generation of the reaction $\bar{p}p \rightarrow \Xi^+ \Xi^- \pi^0$.

State	Mass [MeV/c ²]	Γ [MeV/c ²]
$\Xi(1530)^-$	1535	9.9
$\Xi(1690)^-$	1690	30 (25)
$\Xi(1820)^-$	1823	24 (25)

Table 2: Production and decay branches in the simulation of the signal events. c.c denotes the charge conjugate.

$\bar{p}p \rightarrow$		$\rightarrow \bar{\Xi}^+ \Lambda K^-$
$\bar{p}p \rightarrow$	$\bar{\Xi}^+ \Xi(1690)^-$	$\rightarrow \bar{\Xi}^+ \Lambda K^-$
$\bar{p}p \rightarrow$	$\bar{\Xi}^+ \Xi(1820)^-$	$\rightarrow \bar{\Xi}^+ \Lambda K^-$
$\bar{p}p \rightarrow$		$\rightarrow \Xi^- \bar{\Lambda} K^+$
$\bar{p}p \rightarrow$	$\bar{\Xi}(1690)^+ \Xi^-$	$\rightarrow \Xi^- \bar{\Lambda} K^+$
$\bar{p}p \rightarrow$	$\bar{\Xi}(1820)^+ \Xi^-$	$\rightarrow \Xi^- \bar{\Lambda} K^+$
$\bar{p}p \rightarrow$		$\rightarrow \bar{\Xi}^+ \Xi^- \pi^0$
$\bar{p}p \rightarrow$	$\bar{\Xi}^+ \Xi(1530)^- (+ \text{ c.c.})$	$\rightarrow \bar{\Xi}^+ \Xi^- \pi^0$
$\bar{p}p \rightarrow$	$\bar{\Xi}^+ \Xi(1690)^- (+ \text{ c.c.})$	$\rightarrow \bar{\Xi}^+ \Xi^- \pi^0$
$\bar{p}p \rightarrow$	$\bar{\Xi}^+ \Xi(1820)^- (+ \text{ c.c.})$	$\rightarrow \bar{\Xi}^+ \Xi^- \pi^0$

jectory of a charged particle in a homogeneous magnetic field. Consider the particle is moving along the z-axis. The projection of the trajectory onto the x-y-plane is a circle which can be defined by three hit points inside the detector part. A fourth hit is then a confirmation of the track hypothesis.

4 The Full Decay Tree Fit Procedure

In this section an overview on the method to perform a least-squares fit of a full decay chain is presented. For further information the reader can consult [37].

The presented least-squares fit allows the extraction of all parameters in a decay chain at the same time. This method has been developed for data analysis at the BarBar experiment [37]. It uses a parameterization in terms of vertex position, momentum and decay time of a particle.

The parameterization of the decay tree is chosen as followed:

- Final state particles are represented by their momentum vector (p_x, p_y, p_z) , respectively.
- Intermediate state are modeled by a four-momentum vector (p_x, p_y, p_z, E) and a decay vertex position (x, y, z) . In case the intermediate state is not the initial particle, also the decay time $\theta \equiv l/|\vec{p}|$, where l is decay length, is used as parameter.

Furthermore, two types of constraints have

to be distinguished: the internal constraints, i.e. vertex constraint and momentum conservation constraint, to remove redundant degrees of freedom, and the external constraint constituted by the reconstructed final state particles. The degrees of freedom of the decay tree are formed by the vertex positions and momenta of all involved particles.

The constraints described above are the minimal set of constraints necessary to fit the decay tree starting with the reconstructed final state particles. In addition, it is possible to implement other constraints, e.g. constraining the mass of composites, the production vertex of the decay tree head, and the four-momentum of the head. In principle, missing particles could also be included, if this does not mean that the decay tree is kinematically under-constrained. The order in which the constraints are applied has an impact on the sum of the χ^2 contributions, but with one exception: if all applied constraints are linear, the sum of the χ^2 contributions is not affected by the order of the constraints. Based on this, the external constraints are applied first, followed by all four-momentum conservation constraints. In the last step geometric constraints as well as eventual mass constraints are applied.

In general, the decay tree fit is repeated until the total χ^2 reaches a stable value. In each iteration the parameters are initialized with the results of the previous iteration. In contrast, the covariance matrix is reset for each iteration to its original value.

5 Event Reconstruction

5.1 $\bar{p}p \rightarrow \Xi^+ \Lambda K^- + \text{c.c.}$

In this study, in total about 10 million signal events of the reactions $\bar{p}p \rightarrow \Xi^+ \Lambda K^-$ and $\bar{p}p \rightarrow \Xi^- \bar{\Lambda} K^+$ have been analyzed, containing 40 % $\Xi(1690)^-$ ($\Xi(1690)^+$), 40 % $\Xi(1820)^-$ ($\Xi(1820)^+$), and 20 % continuum content.

Final State Particles

After the track filtering, the final state particle candidates are filled into the corresponding candidates lists. For the selection of the possible candidates no PID information is used. This implies that for a given charge sign each of the corresponding candidates lists are filled with the same candidate. The single candidates differ only in the mass, which is set according to the hypothesis of the corresponding candidate list.

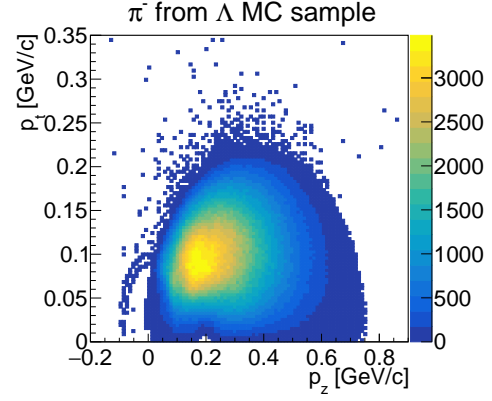
If at least three candidates for each charge sign are available per event, it is marked as "reconstructable". This pre-selection avoids the reconstruction of incomplete signal events.

In the following, the reconstruction efficiency is defined as ratio of MC matched candidates and the number of generated candidates. MC matched means that the reconstructed candidate has a partner in the MC truth list which has the correct event genealogy up to the initial $\bar{p}p$ system. The reconstruction efficiencies achieved for the final state particles are listed in Table 3. The determined statistical error on the reconstruction efficiency is of the order of $\sigma_\epsilon \simeq 0.1\%$.

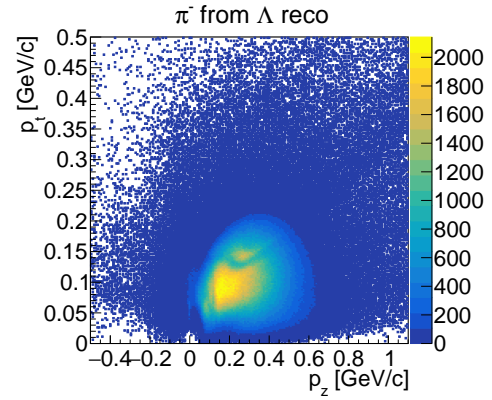
For each final state particle two-dimensional histograms of transverse momentum versus lon-

Table 3: Reconstruction efficiency for the final state particles of $\bar{p}p \rightarrow \Xi^+ \Lambda K^-$ and $\bar{p}p \rightarrow \Xi^- \bar{\Lambda} K^+$.

particle type	eff. [%]	c.c. eff. [%]
π^-	71.2	70.6
π^+ ($\bar{\Lambda}$)	68.6	68.3
π^+ (Ξ^+)	73.7	73.1
K^- (resonance)	84.9	86.7
K^- (continuum)	85.1	86.9
p	88.7	86.2
\bar{p}	82.3	83.4



(a)



(b)

Figure 3: Transverse vs. longitudinal momentum distribution for generated (a) and reconstructed (b) π^- candidates from Λ , requiring that the generated Λ has only two daughters.

gitudinal momentum as well as absolute momentum versus polar angle are generated. As an example, the generated and the reconstructed transverse versus longitudinal momentum distributions for π^- coming from Λ are shown in Figure 3. Here, the generated distributions are used as reference plots to deduce the quality of the reconstruction. For all final state candidates the distributions contain entries outside the kinematically allowed. This could be caused by interactions of the generated particles inside the detector material or with the beam pipe during the propagation. The comparison between the generated and the reconstructed distributions shows that the π^- from the signal events are clearly identifiable. The momentum resolution which is defined as

$$\frac{dp}{p} = \frac{p^{\text{reco}} - p^{\text{MC}}}{p^{\text{MC}}} \quad (1)$$

Table 4: Momentum resolution for the final state particles of $\bar{p}p \rightarrow \Xi^+ \Lambda K^-$ and $\bar{p}p \rightarrow \Xi^- \bar{\Lambda} K^+$ (c.c.). The error on the fit value is dominated by the systematic error which is estimated to be 0.09 %.

particle type	dp/p [%]	c.c. dp/p [%]
π^-	1.61	1.61
π^+ ($\bar{\Lambda}$)	1.64	1.64
π^+ (Ξ^+)	1.48	1.48
K^- (res.)	1.65	1.65
K^- (cont.)	1.66	1.65
p	1.63	1.61
\bar{p}	1.59	1.60

the difference between the reconstructed and the generated (MC) momentum normalized to the generated momentum. The value of the resolution is determined by performing a double Gaussian fit to the resulting distribution and using the width of the inner Gauss fit. By varying the fit parameters, the systematic error is estimated to be 0.09 %. The determined fit values are summarized in Table 4.

Intermediate State Particles

The candidate selection of the intermediate state particles, i.e. $\bar{\Lambda}$, Λ , Ξ^+ and Ξ^- , are similar for each particle type. In the first step, $\bar{\Lambda}$ and Λ are built by combining the daughter particles: \bar{p} and π^+ for $\bar{\Lambda}$, p and π^- for Λ . In the next stage of reconstruction $\bar{\Lambda}$ and an additional π^+ are combined to Ξ^+ as well as Λ and π^- to Ξ^- in the charge conjugate channel. Since the input for the DecayTreeFitter are “raw” candidates, only a coarse pre-selection is done to reduce the number of wrongly combined candidates. For this a symmetric mass window cut of $\pm 0.15 \text{ GeV}/c^2$ around the nominal hyperon mass is applied on the candidate masses. This selection rejects candidates with a mass much higher than the input hyperon mass. All remaining candidates are passed to the next stage of reconstruction.

Full Decay Tree

In the following, the reconstruction of the full decay tree is described. For the final candidate selection a fit of the full decay tree is performed. Within this procedure, described in

section Section 4, the four-momentum conservation of the initial energy and momentum vector

$$P_{\text{ini}} = (0, 0, 4.6, 5.633),$$

as well as the hyperon masses are constraint. Unless otherwise indicated, the results listed below are for the $\Xi^+ \Lambda K^-$ final state.

Since the Ξ resonances decay promptly into a ΛK^- pair or into $\bar{\Lambda} K^+$ in the charge conjugate channel, the reconstruction of the full decay tree is done by combining $\Xi^+ \Lambda K^-$ and $\Xi^- \bar{\Lambda} K^+$, respectively. Subsequently, the candidates are fitted with the DecayTreeFitter implemented in PandaRoot. The fit quality is represented by the χ^2 value and a fit probability is calculated. Figure 4 shows the corresponding distributions. The probability distribution (Fig. 4b) shows a rising behaviour close to the value of one. That indicates that the errors are overestimated for some cases. The fit probability is used as selection criterion for the candidate selection. Here, a cut on $P > 1 \cdot 10^{-4}$ is applied corresponding to a cut on the χ^2 value with $\chi^2 < 43$. Since the fit does not converge or even fails for a significant number of candidates, an additional cut on the fit status is applied to ensure that the fit for the final selected candidates has converged. The final selected sample contains of 277,133

Table 5: Reconstruction efficiency and purity for the final selected signal samples.

Sample	Reco. Eff. [%]	Purity [%]
$\Xi^+ \Lambda K^-$	5.4	97.7
$\Xi^- \bar{\Lambda} K^+$	5.5	97.7

events in case of $\Xi^- \bar{\Lambda} K^+$ and of 283,617 events in case of $\Xi^+ \Lambda K^-$. Table 5 summarizes the achieved reconstruction efficiency and the signal purity for the final selected signal samples. In addition, the ratio between the resonant and the non-resonant decay modes is determined, see Table 6. A comparison with the input values shows, that the fraction for $\Xi(1690)^-$ and $\Xi(1690)^+$ are lower and the fraction for $\Xi(1820)^-$ and $\Xi(1820)^+$ are higher than the input values, while the determine fraction for the continuum contribution is in good agreement with the input. The deviations are within 3σ for all reconstructed resonant states. The DecayTreeFitter uses kinematic fits, like

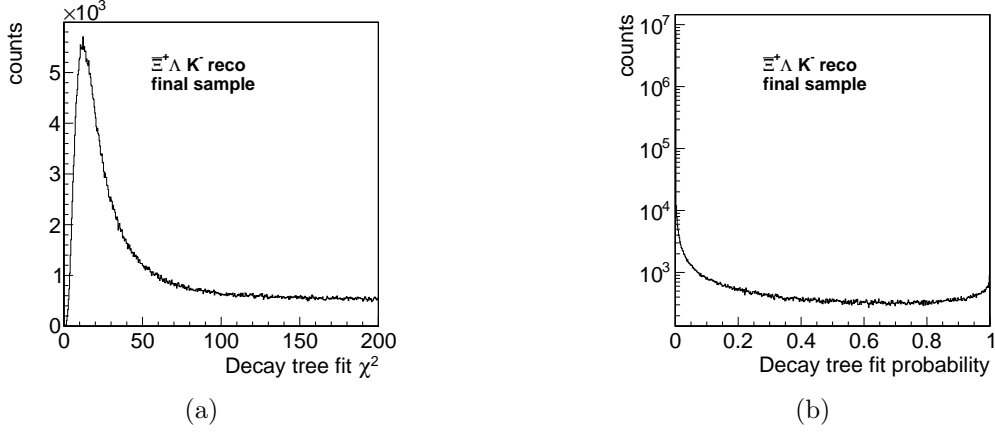


Figure 4: χ^2 (a) and probability (b) distribution for the decay tree fit performed on the $\Xi^+ \Lambda K^-$ sample. The rise of the probability distribution indicates that the errors are overestimated in some cases.

Table 6: Channels and fraction for the $\bar{p}p \rightarrow \Xi^+ \Lambda K^-$ and $\bar{p}p \rightarrow \Xi^- \bar{\Lambda} K^+$ final reconstructed sample (Reco.) and the generated sample (Input).

Channel	reco. [%]	Input [%]
$\Xi^+ \Xi(1690)^-$	37.7 ± 0.8	40
$\Xi^+ \Xi(1820)^-$	42.4 ± 0.8	40
$\Xi^+ \Lambda K^-$	19.9 ± 0.5	20
<hr/>		
$\Xi^- \Xi(1690)^+$	37.8 ± 0.8	40
$\Xi^- \Xi(1820)^+$	42.2 ± 0.8	40
$\Xi^- \bar{\Lambda} K^+$	19.9 ± 0.5	20

Table 7: Momentum resolution for the intermediate state particles of $\bar{p}p \rightarrow \Xi^+ \Lambda K^-$ and $\bar{p}p \rightarrow \Xi^- \bar{\Lambda} K^+$.

Particle	σ [%]	sys. error[%]
Λ	0.777	0.007
$\bar{\Lambda}$	0.803	0.007
Ξ^+	1.30	0.01
<hr/>		
Λ	0.795	0.006
$\bar{\Lambda}$	0.748	0.006
Ξ^-	1.29	0.01

the four-momentum constraint fit, which leads to a correction of the momentum and the energy for each involved candidate to match the initial four-momentum vector. This correction has an impact on the momentum resolution of the candidates. The momentum resolution is evaluated by performing a double Gaussian fit to the relative deviation of the reconstructed and generated total momentum, like described in Section 5.1. Table 7 summarizes the evaluated momentum resolution of the intermediate state particles.

By evaluating the value of the full width at half maximum (FWHM) from the deviation of the reconstructed and the generated decay vertex position, the decay vertex resolution for all three spatial coordinates can be determined. The achieved resolutions for all intermediate state particles are listed in Table 8. Since

the determined FWHM is depending on the chosen bin size, the error on the FWHM is estimated by varying the number of bins of the corresponding histogram. With this procedure, the error is estimated to be about 0.02 mm.

The decay products of the resonance together with the additional hyperon, $\Xi^+ \Lambda K^-$ and $\Xi^- \bar{\Lambda} K^+$, can be defined as three-body final state of the strong interaction, since the involved particles further decay weakly or electromagnetically. In this analysis, $M^2(\Lambda K^-)$ and $M^2(\Xi^+ K^-)$ as well as the squared mass for their charge conjugate particles are used as the axes of the Dalitz plot. The different decay modes of the reaction lead to different distributions within the Dalitz plot. For the continuum production of the three-body final state, the Dalitz plot shows a flat distribution over the entire kinematically

Table 8: FWHM of all three spatial coordinates for the final selected intermediate state particles of $\bar{p}p \rightarrow \Xi^+ \Lambda K^-$ and $\bar{p}p \rightarrow \Xi^- \bar{\Lambda} K^+$.

Particle	x [mm]	y [mm]	z [mm]
$\bar{p}p \rightarrow \Xi^+ \Lambda K^-$			
Λ	0.26	0.22	1.28
$\bar{\Lambda}$	0.30	0.26	1.40
Ξ^+	0.28	0.28	1.20
$\bar{p}p \rightarrow \Xi^- \bar{\Lambda} K^+$			
Λ	0.30	0.26	1.36
$\bar{\Lambda}$	0.26	0.26	1.28
Ξ^-	0.28	0.28	1.20

allowed region. For a contributing resonant process, the resonance will be visible as a band in the Dalitz plot. The Dalitz plot for the $\Xi^+ \Lambda K^-$ final state is shown in Figure 5. Here, the Ξ resonances are visible as vertical bands around the nominal squared mass values. To compare the reconstructed and the generated Dalitz plot, the ratio of the Dalitz plots for the MC truth partners of the reconstructed and the generated candidates is illustrated in Figure 6. The ratio plot shows a uniform distribution. By illustrating the ratio of the generated and reconstructed mass distribution for the ΛK^- sub-system, Figure 7, one can observe a decrease of the reconstruction efficiency by about 20 % towards lower sub-system masses. This loss of efficiency has to be further investigated.

The mass and the width of the resonances are determined by fitting a function containing two

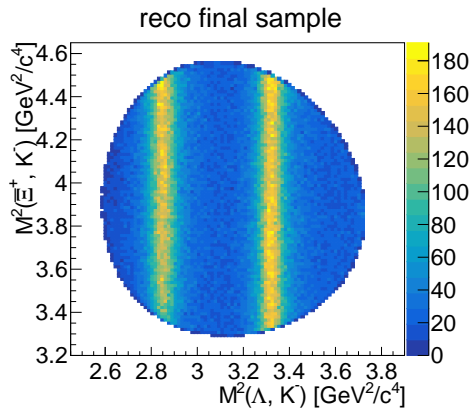


Figure 5: Dalitz plot for the final selected $\Xi^+ \Lambda K^-$ candidates.

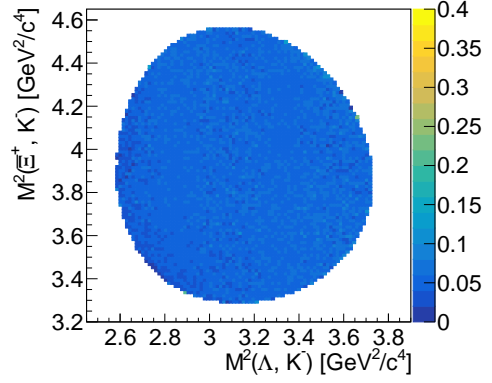


Figure 6: Ratio of the Dalitz Plots for the MC truth partners of the final sample and the generated sample.

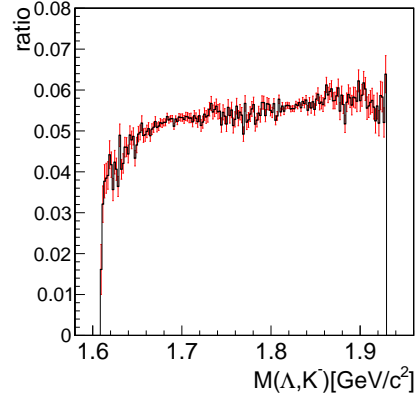


Figure 7: Ratio of the mass distribution for the MC truth partners of the final sample and the generated sample.

Voigt functions [38] and a polynomial to the corresponding mass distributions. The mass distribution of ΛK^- is shown as an example in Figure 8. In this analysis, the best fit result is achieved by fixing the instrumental width σ for both resonances to $\sigma = 0.004 \text{ GeV}/c^2$. This value was determined by calculating the FWHM for the deviation of the final reconstructed and the generated mass distribution. The resulting fit values for the Ξ resonances are summarized in Table 9. Except for the width for $\Xi(1820)^-$ and $\Xi(1820)^+$, the fitted values are consistent with the input values listed in Table 1. The width for $\Xi(1820)^-$ and $\Xi(1820)^+$ agree within 2σ .

An isotropic angular distribution was assumed for the production of the Ξ^+ and Ξ^{*-} as well as for their charge conjugate particles.

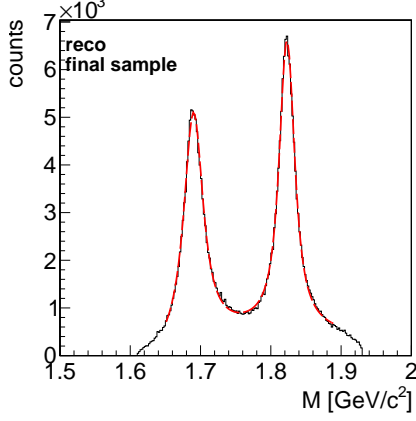


Figure 8: Mass distribution of ΛK^- with fit function containing two Voigt functions and a polynomial.

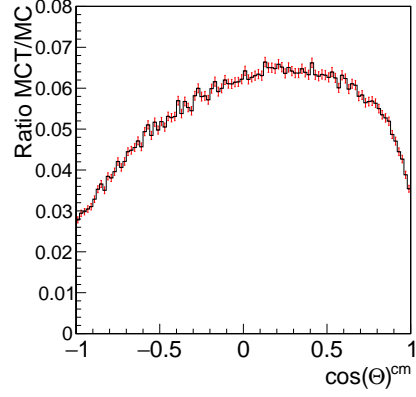


Figure 9: Ratio of the $\cos \theta$ distribution in the center-of-mass frame for the final selected candidates.

Table 9: Fit results for the mass and width of the Ξ resonances determined with a fit function containing two Voigt functions and a polynomial.

	M [MeV/c ²]	Γ [MeV/c ²]
$\Xi(1690)^-$	$1689.99 \pm_{0.09(\text{stat.})}^{0.1(\text{sys.})}$	$30.1 \pm_{0.4(\text{stat.})}^{0.5(\text{sys.})}$
$\Xi(1690)^+$	$1690.16 \pm_{0.08(\text{stat.})}^{0.1(\text{sys.})}$	$30.2 \pm_{0.4(\text{stat.})}^{0.5(\text{sys.})}$
$\Xi(1820)^-$	$1822.98 \pm_{0.06(\text{stat.})}^{0.1(\text{sys.})}$	$22.9 \pm_{0.2(\text{stat.})}^{0.4(\text{sys.})}$
$\Xi(1820)^+$	$1823.12 \pm_{0.06(\text{stat.})}^{0.1(\text{sys.})}$	$22.7 \pm_{0.2(\text{stat.})}^{0.4(\text{sys.})}$

From the ratio of the $\cos \theta$ distribution in the c.m. frame for the MC truth partners of the final selected candidates and the generated candidates, shown in Figure 9, it is possible to deduce the reconstruction efficiency for any center-of-mass angular distribution. The ratio shows a reduced efficiency for particles emitted in forward and backward direction, which is due to the loss of propagated particles inside the beam pipe.

5.2 $\bar{p}p \rightarrow \Xi^+ \Xi^- \pi^0$

9 million signal events, generated according to the decay tree shown in Figure 10 have been analyzed containing a continuum contribution as well as the resonant states $\Xi(1530)^-$, $\Xi(1690)^-$, $\Xi(1820)^-$, and their charge conjugate states. In contrast to the former presented analysis, this study has used a step-by-step reconstruction procedure including geometric and kinematic fits.

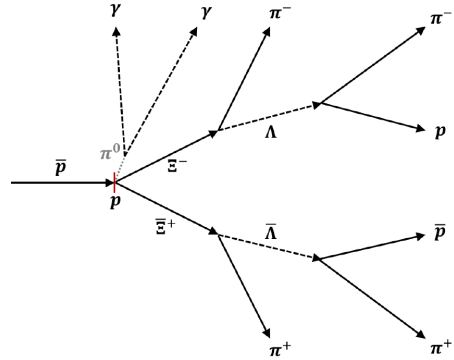


Figure 10: Schematic illustration of the decay tree for the process $\bar{p}p \rightarrow \Xi^+ \Xi^- \pi^0$.

Final States Particles

The reconstruction of the charged final states particles is similar to the reconstruction presented in the previous analysis. However, it should be noted that this study is based on "ideal PID", i.e. the probability for the particles identity is equal to 1 for the MC true species and zero for all other species. In addition, the neutral candidate list is filled whenever hits in the EMC cannot be associated with any charged track. In this analysis, an event is marked as reconstructable, if the event contains the minimum number of entries according to the charged final states, $\bar{p}p\pi^+\pi^+\pi^-\pi^-$ as well as two neutral candidates. The achieved reconstruction efficiency of the charged final state particles is summarized in Table 10.

Table 10: Reconstruction efficiency of the charged final state particles

Particle	Efficiency [%]
p	86.7
\bar{p}	83.7
$\pi^- (\Xi^-)$	75.3
$\pi^- (\Lambda)$	70.6
$\pi^+ (\Xi^+)$	75.7
$\pi^+ (\bar{\Lambda})$	70.9

Intermediate State Particles

The first step is to reconstruct the Λ and $\bar{\Lambda}$ particles. For Λ the list of protons and π^- candidates are combined, for $\bar{\Lambda}$ those of \bar{p} and π^+ . Apart from this the procedure for Λ and $\bar{\Lambda}$ are identical. If not otherwise stated, the following description for Λ applies to the $\bar{\Lambda}$ reconstruction in the same way.

The Λ candidates are first filtered by requiring that the π^-p mass (M_{raw}) is within the following range: $M_{\Lambda} - 0.25 \text{ GeV}/c^2 < M_{\text{raw}} < M_{\Lambda} + 0.25 \text{ GeV}/c^2$. Here the lower bound of the mass window is given by the sum of the masses of the daughter particles. The remaining Λ candidates are subject to a vertex fit, ensuring that the daughter particles have the same origin. To avoid unwanted losses at an early stage of the reconstruction, the threshold for the minimum fit probability is set to 10^{-4} . The vertex fitted Λ candidate is then subject to a mass constraint fit, where the fit probability threshold is again set to 10^{-4} . If more than one Λ candidate fulfills this condition, only the best fit candidate is selected for the following analysis. The signal MC true fraction of the selected Λ and $\bar{\Lambda}$ candidates for this procedure is 91.4% and 91.5%, respectively, meaning that the selected Λ and $\bar{\Lambda}$ candidates contain a fraction of about 8.5% accidental $p\pi^-$ or $\bar{p}\pi^+$ combinations.

The π^- and π^+ candidates used for the reconstruction of Λ and $\bar{\Lambda}$ are removed from the candidate lists in order to avoid double usage at a later stage of the reconstruction.

The procedure to reconstruct the π^0 meson differs from the procedure for the Λ because no useful vertex fit can be performed on the photon daughter.

In the first step of the reconstruction, all members in the neutral candidates list are required to have at least 15 MeV. All pairwise combinations from the neutral candidate list are entered into the π^0 candidate list if the invariant mass of the pair (M_{cand}) is within the following coarse mass window: $m_{\pi^0} - 0.05 \text{ GeV}/c^2 < M_{\text{cand}} < m_{\pi^0} + 0.05 \text{ GeV}/c^2$ is then applied to these candidates. All candidates are subject to a mass constraint fit. A minimum fit probability threshold of 10^{-3} is required. If more than one candidate passes the fit, the candidate with the highest fit probability is selected. Figure 11 shows the pre-fit mass distribution of the selected π^0 candidates.

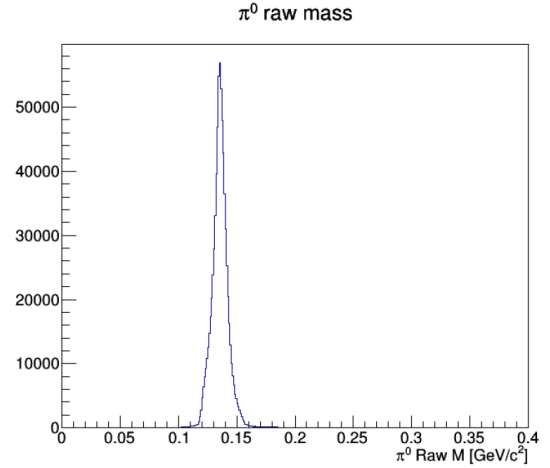


Figure 11: Pre-fit mass distribution of the π^0 candidates passed the mass constraint fit.

Since this study is based on a Monte Carlo simulation the fractions of true and fake π^0 at each stage of the analysis is recorded. The fraction of true π^0 is 48.8%. In addition to the true π^0 candidates whose MC truth partners are the primary π^0 decaying into 2γ , also the so-called "conversion" π^0 candidate, for which one or both of the corresponding decay photons have converted into a e^+e^- pair in the material in front of the EMC, are separately counted. Therefore, the sum of true and "conversion" π^0 candidates is counted as good candidates increasing the fraction of π^0 signal events to 59.2%. The remaining candidates can be interpreted as combinatorial background.

In order to reconstruct Ξ^- and Ξ^+ (anti-) hyperons, candidate pairs of π^- and Λ or π^+ and $\bar{\Lambda}$ are built, respectively. Unless otherwise stated, the description of the Ξ^- reconstruction implicitly includes the reconstruction of Ξ^+ as well. In principle, the same procedure as for the Λ and $\bar{\Lambda}$ reconstruction is used. However, a specific aspect needs to be mentioned. Since one of the daughter particles, Λ or $\bar{\Lambda}$, is a composite system which already passed two fitting processes, here, the vertex and mass constraint fitted candidate lists are used. In a first step, the Ξ^- candidates are filtered by a coarse mass window $M_{\Xi^-} - 0.25 \text{ GeV}/c^2 < M_{\text{raw}} < M_{\Xi^-} + 0.25 \text{ GeV}/c^2$, where the lower bound of the mass window is given by the sum mass of the daughter particles $M_{\Lambda} + M_{\pi^-}$. A vertex fit is applied to the remaining candidates and the lower fit probability is set to 10^{-4} . Subsequently, a mass constraint fit is applied to the vertex fitted Ξ^- candidates. Again the lower fit probability threshold is set to 10^{-4} . After the mass constraint fit, the mass distributions of Ξ^- and Ξ^+ should show delta-functions. However, it can be observed that for about 1% of the selected Ξ^- candidates the mass constraint is not respected, so that entries in the unphysical region can occur in the further reconstruction process. Further investigations have shown that these events cannot be removed with a stricter cut on the fit probability. If there is more than one Ξ^- candidate per event passing the mass constraint fit, only the best fit candidate is selected for the following analysis. At this stage of the reconstruction, the sample purity is 95.3% for both Ξ^- and Ξ^+ .

Reconstruction of the $\Xi^+\Xi^-$ Vertex

Since Ξ^- and Ξ^+ have a relatively short decay length $c\tau = 4.91 \text{ cm}$, the corresponding tracks are not expected to deliver a sufficient number of hits in the MVD, meaning that Ξ^- and Ξ^+ are not reconstructable directly. Both particles are created in the $\bar{p}p$ collisions and thus their tracks must meet at the interaction point. Although they are not kinematically related by a common mother particle, the reconstructed vertex and mass fitted Ξ^- and Ξ^+ candidate pair is combined to a $\Xi\Xi$ candidate

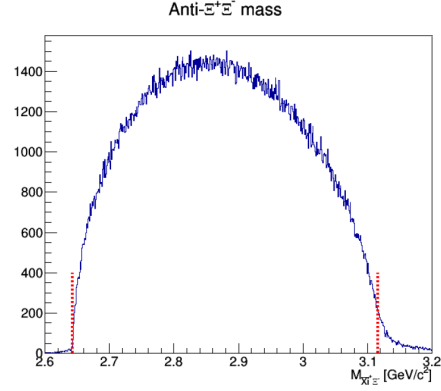


Figure 12: Mass distribution of the vertex fitted $\Xi\Xi$ candidates. The red dotted lines denote the kinematic limits. From the generated events a uniform distribution is expected.

on which a vertex fit is performed. A lower threshold of 10^{-4} for the fit probability was applied. The mass distribution of the fitted $\Xi\Xi$ candidates is shown in Figure 12. The lower kinematic limit is given by twice the Ξ^- mass $2M_{\Xi^-} = 2.643 \text{ GeV}/c^2$ and the upper limit by $\sqrt{s} - m_{\pi^0}$. These limits are indicated by the read dashed lines in the Figure 12. Entries below the allowed region are due to unphysical masses of the mass constraint fitted Ξ^- and Ξ^+ candidates, whereas entries above are caused by deviations of the $\Xi\Xi$ daughter three-momentum vectors from the true values.

Reconstruction of the $\Xi^+\Xi^-\pi^0$ System

In the last step of the analysis, the complete $\Xi^+\Xi^-\pi^0$ system is combined. On this system a kinematic four-constraint fit (4C-fit) to the four-momentum vector of the initial $\bar{p}p$ system is performed for which a lower probability threshold of 10^{-4} is applied. It is observed, that the constraint to the initial $\bar{p}p$ four-momentum is not perfectly fulfilled. In order to remove those events, it is required that the overall mass (M) in the c.m. is within the range of $3.24 \text{ GeV}/c^2 < M < 3.26 \text{ GeV}/c^2$. The final selected signal sample contains around $1.6 \cdot 10^5$ reconstructed events. The described selection scheme leads to a reconstruction efficiency of 3.5%. The most significant losses occur in the reconstruction of π^0 mesons. The signal purity of the final selected $\Xi^+\Xi^-\pi^0$ candidates is

94.1%. In order to estimate the reconstructed signal event rate, the number of remaining signal events needs to be multiplied by the product of all branching fractions of 0.4026 within the decay tree, the luminosity and the cross section.

The Dalitz plots for the final selected $\Xi^+\Xi^-\pi^0$ are shown in Figure 13. The contributing resonances in are clearly observable as bands in Figure 13b. The mass and width of resonances are determined by fitting a function, containing three Voigt functions as well as functions to describe the continuum and the crossed channel components of the recon-

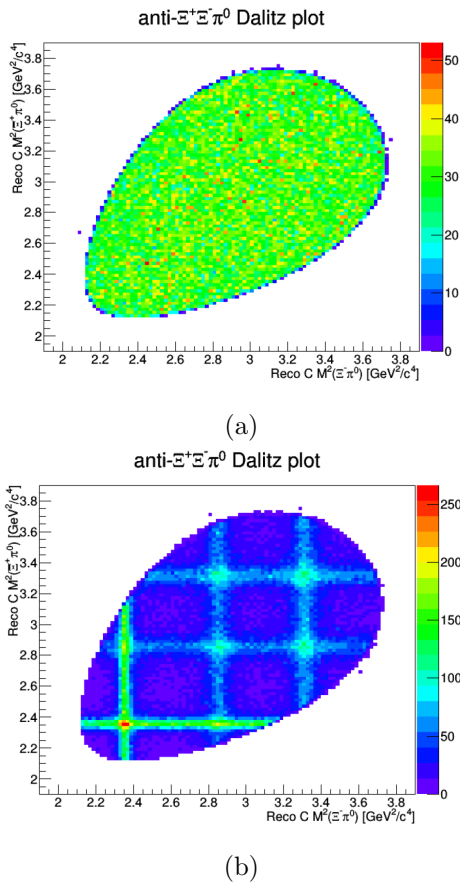


Figure 13: Dalitz plot for the final selection $\Xi^+\Xi^-\pi^0$ from the continuum contribution (a) and with resonance contribution only (b).

structed mass distributions of $\Xi^-\pi^0$ and $\Xi^+\pi^0$. As an example, the mass distribution of the final selected $\Xi^-\pi^0$ sub-system as well as the corresponding fit function are shown in Figure 14. Table 11 summarized the obtained masses and widths of the contributing resonances. One has to note that for $\bar{p}p$

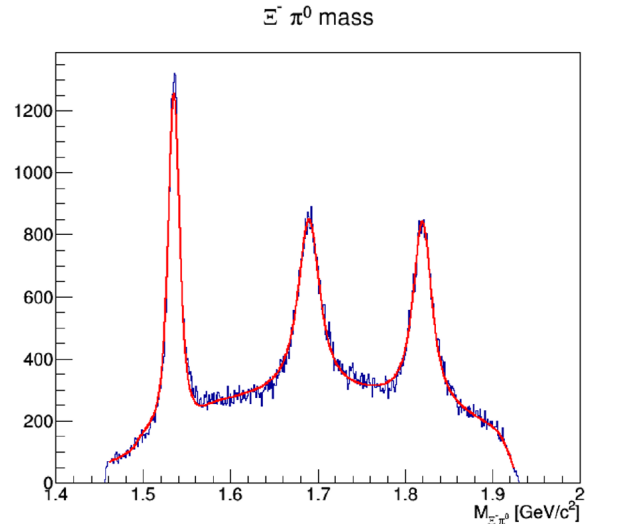


Figure 14: Mass distribution of the final selected $\Xi^-\pi^0$ sub-system. The fit function used to determine the mass and the width of the contributing resonances is shown in red.

$\rightarrow \Xi^+\Xi^-\pi^0$ the input value $M(\Xi(1820)) = 1.820 \text{ GeV}/c^2$ was slightly lower compared to the input value $M(\Xi(1820)) = 1.823 \text{ GeV}/c^2$ used for the other study. The determined masses for $\Xi(1530)^+$, $\Xi(1690)^-$, $\Xi(1690)^+$, $\Xi(1820)^-$, and $\Xi(1820)^+$ as well as the widths for $\Xi(1530)^-$ are in good agreement with the input values shown in Table 1. But the mass for $\Xi(1530)^-$ and all widths of the resonances deviate significantly from the input values. The determined errors are purely statistical. A detailed study of systematic errors is needed.

Table 11: Fit results for the reconstructed masses and widths of the contribution resonances.

	Mass [MeV/c ²]	Γ [MeV/c ²]
$\Xi(1530)^-$	1535.3 ± 0.1	9.9 ± 0.2
$\Xi(1690)^-$	1690.1 ± 0.2	26.9 ± 0.7
$\Xi(1820)^-$	1820.2 ± 0.1	22.2 ± 0.6
$\Xi(1530)^+$	1535.1 ± 0.1	9.5 ± 0.2
$\Xi(1690)^+$	1689.8 ± 0.2	26.9 ± 0.7
$\Xi(1820)^+$	1820.1 ± 0.2	22.6 ± 0.6

6 Background Studies

In addition to the study of the signal channel, a study of hadronic background events is performed. Beside the hadronic background, other sources of potential background are processes ending in similar final states, e.g. $\bar{p}p \rightarrow p\bar{p}\pi^+\pi^+\pi^-\pi^-K^+K^-$ for $\bar{p}p \rightarrow \bar{\Xi}^+\Lambda K^-$ and $\bar{p}p \rightarrow p\bar{p}\pi^+\pi^+\pi^-\pi^-\pi^0$ for $\bar{p}p \rightarrow \bar{\Xi}^+\Xi^-\pi^0$. Here, data samples were generated with the Dual Parton Model [39] based generator DPM including only inelastic processes. These events were subjects to the same analysis strategy used for the signal events.

For the study of $\bar{p}p \rightarrow \bar{\Xi}^+\Lambda K^-$, 100 million generated background events were analyzed. No event out of these 100 million events survived the analysis procedure.

Due to another software version used in the study of $\bar{p}p \rightarrow \bar{\Xi}^+\Xi^-\pi^0$, 22 million generated DPM events were subject to the same selection strategy as the signal events. Two events remained in the event sample after applying the full analysis procedure. Further studies showed, that these events could be completely removed by restricting the Λ and $\bar{\Lambda}$ respective proper time ($ct_{\Lambda,\bar{\Lambda}}$) values and the distance between the Ξ^- and $\bar{\Xi}^+$ decay vertices $d_{\Xi^-\bar{\Xi}^+}$. By requiring $3\text{ mm} < ct_{\Lambda,\bar{\Lambda}} < 1\text{ m}$ and $d_{\Xi^-\bar{\Xi}^+} < 2\text{ mm}$ the number of signal events is reduced by 8.4%, corresponding to a remaining signal reconstruction efficiency of 3.0%.

The non-observation of background events corresponds to a 90% confidence upper limit of 2.3 events, which is used to calculate a lower limit for the signal-to-background ratio as well as for the signal significance. The signal-to-background ratio is given by

$$\frac{S}{B} = \frac{\sigma_{\text{sig}} \cdot \epsilon_{\text{sig}} \cdot b_{\text{sig}}}{\sigma_{\text{bg}} \cdot \epsilon_{\text{bg}}}, \quad (2)$$

where σ_{sig} and σ_{bg} are the signal and background cross sections, respectively, b_{sig} is the total branching ratio of signal events, and ϵ_{sig} and ϵ_{bg} are the respective reconstruction efficiencies for signal and background. Since the signal cross sections has not yet been measured, for the $\bar{\Xi}^+\Lambda K^-$ signal final state, it is assumed to be $\sigma_{\text{sig}} = 1\mu\text{b}$ and for $\bar{\Xi}^+\Xi^-\pi^0$ to be $2\mu\text{b}$, since in experimental studies the cross section for the $\bar{\Xi}^+\Xi^-\pi^0$ ground was determined to be higher than the cross section for

the $\bar{\Xi}^+\Lambda K^-$ ground state [4]. Furthermore, the inelastic $\bar{p}p$ cross section at a beam momentum of 4.6 GeV/c is $\sigma_{\text{bg}} = 50\text{ mb}$ [35]. During the generation of the signal events, the branching ratio of Λ and $\bar{\Lambda}$ was set to 100% for the decay $\Lambda \rightarrow p + \pi^-$ and $\bar{\Lambda} \rightarrow \bar{p} + \pi^+$. For the following calculations this ratio has to be corrected with the true branching ratio of the full signal. This leads to $b_{\text{sig}} = b_{\Lambda}^2 = 0.4083$ for both final states investigated here.

For the signal events, the reconstruction efficiency is $\epsilon_{\text{sig}} = 5.4\%$ for both $\bar{\Xi}^+\Lambda K^-$ and $\Xi^-\bar{\Lambda}K^+$, and $\epsilon_{\text{sig}} = 3.0\%$ for $\bar{\Xi}^+\Xi^-\pi^0$. The significance of the signal S_{sig} is given by

$$S_{\text{sig}} = \frac{N_{\text{sig}}}{\sqrt{N_{\text{sig}} + N_{\text{bg}} \cdot F_{\text{bg}}}}, \quad (3)$$

where F_{bg} denotes a scaling factor which corrects the number of background events according to the number of signal events, since the generated ratio for signal and background does not reflect the cross sections. The scaling factor is given by

$$F_{\text{bg}} = \frac{N_{\text{sig}}^{\text{gen}} \cdot \sigma_{\text{bg}}}{N_{\text{bg}}^{\text{gen}} \cdot \sigma_{\text{sig}} \cdot b_{\text{sig}}}, \quad (4)$$

where $N_{\text{sig}}^{\text{gen}}$ and $N_{\text{bg}}^{\text{gen}}$ are the number of generated signal and background events, respectively. The calculated signal-to-background ratio and signal significance for each investigated channel are summarized in Table 12. In addition, the same calculations for a factor 10 smaller cross section are included in the table which gives the lower limit for the case, that the estimated cross is off by an order of magnitude.

Table 12: Signal-to-background ratio and signal significance. In addition to the assumed cross sections, calculations for a cross section of a factor 10 less are done.

	σ_{sig}	$\bar{\Xi}^+\Lambda K^-$ (&c.c.)	$\bar{\Xi}^+\Xi^-\pi^0$
S/B	$\sim 1\mu\text{b}$	> 19.1	> 4.6
S_{sig}	$\sim 1\mu\text{b}$	> 513	> 349
S/B	$\sim 0.1\mu\text{b}$	> 1.91	> 0.4
S_{sig}	$\sim 0.1\mu\text{b}$	> 428	> 216

7 Results and Discussion

In the previous section the feasibility study of the reactions $\bar{p}p \rightarrow \bar{\Xi}^+ \Lambda K^-$, $\bar{p}p \rightarrow \Xi^- \bar{\Lambda} K^+$, and $\bar{p}p \rightarrow \bar{\Xi}^+ \Xi^- \pi^0$ was described. Different approaches were used for both studies: a fit of the full decay tree for $\bar{p}p \rightarrow \bar{\Xi}^+ \Lambda K^-$ and its charge conjugate channel, and a step-by-step fit procedure for $\bar{p}p \rightarrow \bar{\Xi}^+ \Xi^- \pi^0$.

In absence of experimental data and theoretical predictions for the angular distribution of the signal events, a uniform phase space distribution was assumed. This assumption is reasonable, since the amount of energy above the threshold is low for both channels and both strange valence quarks have been pair produced from the sea. Here, this simplification assures, that the produced Ξ^- and $\bar{\Xi}^+$ hyperons are underlying the same detector acceptance. An ideal pattern recognition was used for the track reconstruction in both analyses, since a realistic tracking algorithm for secondary tracks is currently not available. Therefore, a track filter was introduced to make the charged final state particle selection more realistic.

The single particle reconstruction efficiency for the charged final state particles is between 68 % and 89 %. Since the study of $\bar{p}p \rightarrow \bar{\Xi}^+ \Xi^- \pi^0$ used ideal PID, the reconstruction efficiency is expected to be slightly higher compared to the study with realistic PID. A comparison of ideal and open PID for $\bar{p}p \rightarrow \bar{\Xi}^+ \Lambda K^-$ has shown that the reconstruction efficiency for the full decay tree is reduced by $\sim 20\%$ when realistic PID.

The intermediate state particles are reconstructed differently in both methods. The first analysis applies a coarse mass window symmetrically around the nominal hyperon mass. For $\bar{p}p \rightarrow \bar{\Xi}^+ \Xi^- \pi^0$ an additional vertex fit and mass constraint fit is applied to each candidate.

With the resulting candidates, the three-body systems $\bar{\Xi}^+ \Lambda K^-$, $\Xi^- \bar{\Lambda} K^+$, and $\bar{\Xi}^+ \Xi^- \pi^0$ are calculated. $\bar{\Xi}^+ \Lambda K^-$ and $\Xi^- \bar{\Lambda} K^+$ are subsequently fitted with the DecayTreeFitter. In this analysis a reconstruction efficiency of $\sim 5\%$ is achieved for each channel. The achieved sample purity is 97.7 % for each channel, implying that the genealogy of the signal is suppressing the combinatorial back-

ground efficiently. The $\bar{\Xi}^+ \Xi^- \pi^0$ candidates are subject to a four-constraint fit to the initial $\bar{p}p$ four-momentum vector. This selection scheme leads to a total reconstruction efficiency of 3.5 % and a sample purity of 94.1 %.

for several reasons a direct comparison of the reconstruction efficiencies achieved with the two methods could be misleading. First off: the implemented DecayTreeFitter needed a newer version of the software framework compared to the step-by-step fitting procedure. In addition, the channel $\bar{p}p \rightarrow \bar{\Xi}^+ \Xi^- \pi^0$ includes a π^0 meson which has a low reconstruction efficiency, since the selection is only based on obtaining the best pair invariant mass of the neutral particles.

In both studies, the reconstructed resonance masses are in good agreement with the input values.

With the assumed cross section of $1\mu\text{b}$ for each considered final state, $\bar{\Xi}^+ \Lambda K^-$ and $\Xi^- \bar{\Lambda} K^+$, the determined reconstruction efficiencies and the initial luminosity of $L = 10^{31}\text{cm}^{-2}\text{s}^{-1}$, the expected reconstructed number of events is 38,500 per day. For the $\bar{\Xi}^+ \Xi^- \pi^0$ final state a cross section of $2\mu\text{b}$ is assumed. With the corresponding reconstruction efficiency and the initial luminosity, 22,800 reconstructed events are expected per day. These rates correspond to about 7 days ($\bar{\Xi}^+ \Xi^- \pi^0$) and 15 days ($\bar{\Xi}^+ \Lambda K^-$ and $\Xi^- \bar{\Lambda} K^+$) of data taking to collect data samples with the same size of the reconstructed samples shown in this report.

For the study of the hadronic background the same analysis strategies were used as for the signal, leading to no surviving event out of 100 million generated background events for the $\bar{\Xi}^+ \Lambda K^-$ and $\Xi^- \bar{\Lambda} K^+$ final states. For the $\bar{\Xi}^+ \Xi^- \pi^0$ final state two events out of 22 million background events survived the applied cuts. Additional selection based on the distance between the vertices removed all background, but also reduced the overall signal efficiency to 3 %. The background studies showed that on a 90 % confidence level a signal-to-background ratio of $S/B > 19.1$ for $\bar{\Xi}^+ \Lambda K^-$, $S/B > 19.5$ for $\Xi^- \bar{\Lambda} K^+$ and $S/B > 4.6$ for $\bar{\Xi}^+ \Xi^- \pi^0$ could be achieved. The lower limit for the signal significance is $S_{\text{sig}} > 513$ for $\bar{\Xi}^+ \Lambda K^-$, $S_{\text{sig}} > 507$ for $\Xi^- \bar{\Lambda} K^+$ and $S_{\text{sig}} > 349$ for $\bar{\Xi}^+ \Xi^- \pi^0$. To deduce a more reliable value for

the signal-to-background ratio and the signal significance, in future studies by at least a factor 10 larger background sample should be generated and analyzed.

The decay tree includes six final state particles in case of $\bar{p}p \rightarrow \bar{\Xi}^+ \Lambda K^-$ (+ c.c.) and eight for $\bar{p}p \rightarrow \bar{\Xi}^+ \Xi^- \pi^0$. Here, the combined acceptance of the final state particles is limiting the reconstruction efficiency. In the study of $\bar{p}p \rightarrow \bar{\Xi}^+ \Xi^- \pi^0$ the most limiting factor is the reconstruction of $\pi^0 \rightarrow \gamma\gamma$, since the reconstruction efficiency for π^0 is only about 40 %.

Both analyses demonstrate that the experimental study of the process $\bar{p}p \rightarrow \bar{\Xi}^+ \Lambda K^-$, its charge conjugate channel and $\bar{p}p \rightarrow \bar{\Xi}^+ \Xi^- \pi^0$, including also resonant baryon states, is feasible with the PANDA detector.

8 Summary and Outlook

A first step has been done in investigating the feasibility of studying the ΛK and the $\Xi\pi$ decay of Ξ resonances with the PANDA detector in the reaction $\bar{p}p \rightarrow \bar{\Xi}^+ \Xi^{*-}$ and its charge conjugate channel at an antiproton beam momentum of 4.6 GeV/c.

In the $\bar{\Xi}^+ \Lambda K^-$ study, a reconstruction efficiency of about 5 % has been achieved with a sample purity of 98 %. The total reconstruction efficiency corresponds to 277,133 $\bar{\Xi}^+ \Lambda K^-$ events and 283,617 $\Xi^- \bar{\Lambda} K^+$ events. Assuming an initial luminosity $L = 10^{31} \text{ cm}^{-2} \text{ s}^{-1}$, the number of final selected signal events can be collected within 15 days of data taking. 100 million generated DPM background events were subject to the same selection strategy. No event out of 100 million survived, so that on a 90 % confidence level a lower limit for the signal-to-background ratio of 513 for $\bar{\Xi}^+ \Lambda K^-$ and 507 $\Xi^- \bar{\Lambda} K^+$ has been determined.

In the analysis of the $\bar{\Xi}^+ \Xi^- \pi^0$ signal events the obtained total reconstruction efficiency is 3.5 %, before any cut on the (anti-)hyperon decay vertex position with respect to the interaction point. The sample purity of the final selected sample is ~ 94 %. The fake combinations in the sample are dominated by accidental combinations of neutral candidates in the reconstruction of the π^0 mesons. The

total reconstruction efficiency of the signal events corresponds to about $1.6 \cdot 10^5$ events which can be collected in 7 days of data taking at the luminosity of $10^{31} \text{ cm}^{-2} \text{ s}^{-1}$. The identical analysis of 22 million DPM background events results in two events surviving the applied cuts. These events can be removed by requiring a proper time of Λ and $\bar{\Lambda}$ larger than 3 mm and a separation of more than 2 mm between the Ξ^- and $\bar{\Xi}^+$ decay vertex. The additional restrictions reduce the signal reconstruction efficiency to 3.0 %. A lower limit for the signal-to-background ratio is deduced to be larger than 4.6, and the signal significance to be larger than 349.

The discussion in the previous chapter shows various steps that should be included in the analyzes presented in the future. On point refers to the usage of the ideal tracking algorithm. As soon as a realistic tracking algorithm for secondary particles is available, both studies have to be redone. The second point is the selection of the final state particles. The impact of the various PID selection criteria on the total reconstruction efficiency, the sample purity as well as on the signal-to-background ratio and the signal significance should be investigated. Furthermore, the model dependency of the background events should be reduced by comparing the results to the output of the background generators.

A major goal of the Ξ spectroscopy program at PANDA is the determination of the spin and parity quantum numbers of the Ξ states. Therefore, a partial wave analysis (PWA) of the reconstructed three-body has to be performed. First investigations on a PWA tool which can be combined with a PandaRoot simulation and analysis are ongoing [40].

References

- [1] Wilson, K. G. , Phys. Rev. D **10**, p. 2445. 1974.
- [2] Weinberg, S. , Phys. Letter B **251**, p. 288–292. 1990.
- [3] PANDA Collaboration (Erni, W. *et al.*) , arXiv:0903.3905. 2009.
- [4] Musgrave, B. *et al.* , Il Nuovo Cimento **35**, p. 735–758. 1965.
- [5] FAIR – Facility for Antiproton and Ion Research. Online. URL: <https://fair-center.eu/>.
- [6] Schütt, P. *et al.* , FAIR Operation Modes. 2016. URL: <https://indico.gsi.de/event/7647/contribution/23/material/0/0.pdf>.
- [7] Lehrach, A. *et al.* , Nucl Inst. and Meth. A **561**, pp. 289–296. 2006.
- [8] PANDA Collaboration. , RN-DET-2017-001: General PANDA material. Release Note. 2017.
- [9] Panda Collaboration. TDR for the PANDA Internal Targets. 2012. URL: https://panda.gsi.de/system/files/user_uploads/u.kurilla/RE-TDR-2012-002.pdf.
- [10] Panda Collaboration. TDR for the PANDA Micro Vertex Detector. 2011. URL: https://panda.gsi.de/system/files/user_uploads/u.kurilla/RE-TDR-2011-001.pdf.
- [11] Panda Collaboration. TDR for the PANDA Straw Tube Tracker. 2012. DOI: 10.1140/epja/i2013-13025-8.
- [12] Panda Collaboration. TDR for the PANDA Solenoid and Dipole Spectrometer Magnets. 2009. URL: <https://arxiv.org/abs/0907.0169>.
- [13] Panda Collaboration. TDR for the PANDA Forward Tracker. 2018. URL: https://panda.gsi.de/system/files/user_uploads/admin/RE-TDR-2017-001.pdf.
- [14] Panda Collaboration. TDR for the PANDA Barrel DIRC Detector. 2017.
- [15] Panda Collaboration. TDR for the PANDA Barrel Time of Flight. 2018. URL: https://panda.gsi.de/system/files/user_uploads/ken.suzuki/RE-TDR-2016-003_0.pdf.
- [16] Panda Collaboration. TDR for the PANDA Forward Time of Flight. 2018. URL: https://panda.gsi.de/system/files/user_uploads/admin/RE-TDR-2016-004.pdf.
- [17] Panda collaboration. TDR for the PANDA Muon System. 2012. URL: https://panda.gsi.de/system/files/user_uploads/u.kurilla/RE-TDR-2012-003.pdf.
- [18] Panda Collaboration. TDR for PANDA Electromagnetic Calorimeter. 2008. URL: <https://arxiv.org/pdf/0810.1216.pdf>.
- [19] Panda Collaboration. TDR for the Panda Forward Spectrometer Calorimeter. 2017. URL: <https://arxiv.org/pdf/1704.02713.pdf>.
- [20] Panda Collaboration. TDR for the PANDA Luminosity Detector. 2017.
- [21] Brun, R. and Rademakers, F. , Nucl. Inst. and Meth. A **389**, p. 81–86. 1997.
- [22] Hrivnacova, I. *et al.* , arXiv:cs/0306005. 2003.
- [23] Al-Turany, M. *et al.* , Journal of Physics: Conference Series **396**, 022001. 2012.
- [24] Spataro, S. , Journal of Physics: Conference Series **331**, 032031. 2011.
- [25] Brun, R. *et al.* , GEANT Detector Description and Simulation Tool (Version 3.21). 1993.
- [26] Agostinelli, S. *et al.* , Nucl. Instr. and Meth. A **506**, p. 250–303. 2003.
- [27] Lange, D. J. , Nucl. Instr. and Meth. A **462**, p.152–155. 2001.
- [28] A. Capella. , Perspectives in the Structure of Hadronic Systems, p. 287–310. 1994.
- [29] Bass, S. *et al.* , Progress in Particle and Nuclear Physics **41**, p. 255–369. 1998.
- [30] Sjöstrand, T. , Computer Physics Commun. **101**, p. 18. 1997.

- [31] Ferrari, A. *et al.* , FLUKA: A multi-particle transport code (Program version 2005). 2005.
- [32] Rauch, J. and Schlüter, T. , Journal of Physics: Conference Series **608**, 012042. 2015.
- [33] Fontana, A. *et al.* , Journal of Physics: Conference Series **119**, 032018. IOP Publishing, 2008.
- [34] Lange, D. J. , Nucl. Inst. and Meth. A **462** ,p. 152–155. 2001.
- [35] Tanabashi, M. *et al.* (Particle Data Group). , Phys. Rev. D **98**, 030001. 2018.
- [36] Flaminio, V. *et al.* , CERN-HERA-84-01. 1984.
- [37] Hulsbergen, W. D. , Nucl. Instr. and Meth. A **552**, p. 566–575. 2005.
- [38] Armstrong, B.H. J Quant Spectrosc Radiat Transf **7**, pp. 61–88. 1967.
- [39] Capella, A. , Perspectives in the Structure of Hadronic Systems, p. 287–310. 1994.
- [40] Pütz, J. PhD Thesis, Rheinische Friedrich-Wilhelms-Universität Bonn. 2020. URL: <https://hss.ulb.uni-bonn.de/2020/5747/5747.htm>.